COMMUNICATION

Check for updates

Incorporating a naphthalene diimide polymer into a fullerene electron-transport layer to improve the fracture energy of perovskite solar cells

Matteo R. S. Poma,[a] Yadong Zhang,[b] Muzhi(Charles) Li,[c] Kaitian Mao,[b] Ryan A. DeCrescent, [b] Stephen Barlow, [b] Nicholas Rolston, [cd] Seth R. Marder [*abef] and Michael D. McGehee [*abe]

By blending a naphthalene diimide polymer into C_{60}, we made a solution-processed electron-transport layer (ETL) for perovskite solar cells with fracture energies of 1.25 J m^{-2}, over 3× higher than that of thermally evaporated C_{60}. Fracture energies were measured in a double cantilever beam configuration, and fracture surface images showed a fracture location near the ETL/perovskite interface, indicating a toughening of the interface between the ETL and Ag. We show that this modification to the ETL has no adverse effect on solar cell performance, and highlight the additional benefit of reduced parasitic absorption; a finding relevant for tandem solar cells.

Broader context

Perovskite solar cells (PSCs) exceed efficiencies of 26% at the lab scale and are a promising technology to assist in the global effort to reduce greenhouse gas emissions from energy production. In the past decade, devices have been tuned to have high phase stability, thermal stability, and are steadily seeing longer lifetimes. However, at least one significant hurdle to commercialization still exists: the mechanical weakness and low fracture energy of individual layers and interfaces within the device. C_{60}, a common electron transport layer (ETL) in *p-i-n* PSCs, is known to have a very low fracture energy (G_c), yet there have not been significant efforts to find a cost-effective solution that maintains the desirable electronic properties of C_{60} while improving the mechanical toughness of the material. Although fullerene polymerization would boost the fracture energy, chemical modification of C_{60} is likely too expensive to be a viable option for industry. We demonstrate that blending C_{60} with an electron-transporting polymer increases fracture energy by over 3× compared to pure C_{60}, while preserving device performance. Our optimized ETLs have an average G_c of 1.25 J m^{-2}, making this a safe option to bring mechanically robust PSCs to commercialization without adversely affecting device efficiency.

Introduction

C_{60} and its derivatives are the most widely used electron-transport layer (ETL) materials for high-efficiency inverted (*p-i-n*) perovskite solar cells (PSCs). C_{60} has enabled record-breaking power conversion efficiencies (PCEs) exceeding 26%.[1,2] Its use in ETLs for low-bandgap (<1.6 eV) PSCs is in part because its electron affinity is well matched to that of the perovskite, enabling efficient charge extraction, and its high ionization energy, which is beneficial for hole blocking.[3] Despite enabling high PCEs, C_{60} has at least two major drawbacks: it is mechanically weak, and is often the second most expensive layer in the entire device stack, even with a thickness of only 25 nm.[4–8]

[a]Materials Science and Engineering Program, University of Colorado Boulder, Boulder, Colorado 80303, USA. E-mail: michael.mcgehee@colorado.edu

[b]Renewable and Sustainable Energy Institute, University of Colorado Boulder, Boulder, Colorado 80309, USA

[c]Materials Science and Engineering, Fulton Schools of Engineering, Arizona State University, Tempe, Arizona 85287, USA

[d]School of Electrical, Computer and Energy Engineering, Arizona State University, Tempe, Arizona 85281, USA

[e]Department of Chemical and Biological Engineering, University of Colorado Boulder, Boulder, Colorado 80303, USA

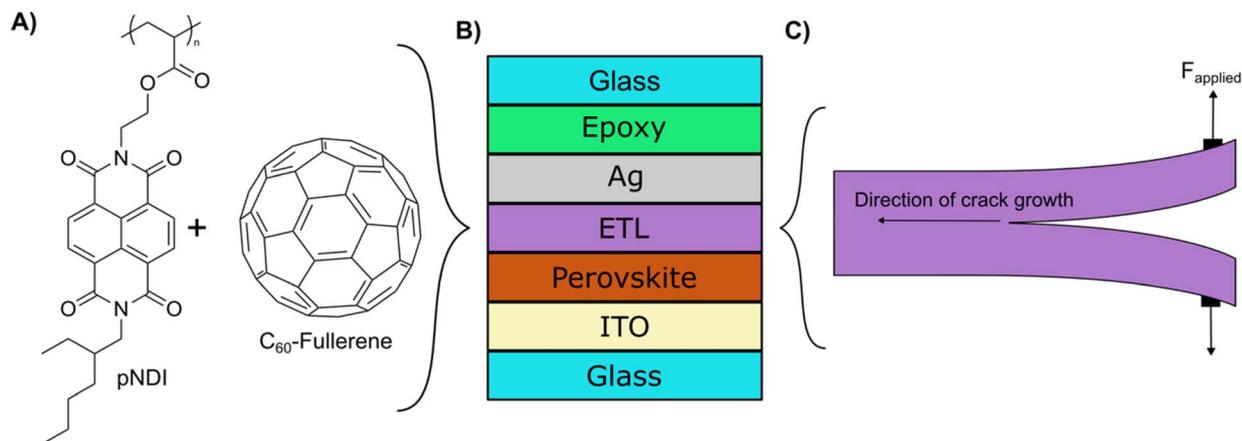*[f]Department of Chemistry, University of Colorado Boulder, Boulder, Colorado 80303, USA*

Every layer and interface in a solar cell must be mechanically tough because, under real-world, outdoor conditions, panels may experience stresses during thermal cycling that arise from mismatches in thermal expansion coefficients of the various components in the panel or from applied mechanical loads.[9] The mechanical bonding of a thin layer or material stack can be quantified by its fracture energy (G_c), a quantitative measure of the energy required to propagate a crack in the bulk material or at the interface. C_{60} and many of its derivatives have low fracture energies of approximately 0.3 J m^{-2} because the molecules are quite large, spherical, and held together only by weak van der Waals forces.[5] This low G_c often leads to mechanical failure in the form of cracking in the ETL and delamination at interfaces.[4–6] Researchers have also observed the failure of photovoltaic modules during outdoor testing due to C_{60} delamination, highlighting the need for a solution.[10] Some G_c improvements have been made in C_{60}-based ETLs. For example, You *et al.* modified C_{60} into an ionic salt with enhanced

Fig. 1 (A) Structures of pNDI and C_{60}. (B) Sample structure for double-cantilever beam fracture energy measurements. Device architecture: ITO//Me4PACz:6dPA//1.55 eV PVK//[evaporated C_{60} or x-pNDI-C_{60}]//PDADI//BCP//Ag. (C) Schematic of cracking in the ETL film during a DCB test.

molecular packing that improved the fracture energy to 1.43 J m^{-2}.[4,11] However, a potentially more economical alternative to modifying the C_{60} directly is to make a composite material comprising C_{60} and a separate molecular or polymeric species. For example, an electron-transporting polymer has been used as an additive at low concentrations to improve the solution processability of C_{60} by inhibiting the aggregation of C_{60} molecules in solution.[12] However, changes in mechanical properties of the ETL were not reported, and the complex structure of the specific polymer used, which requires a 12-step synthesis, may make it too costly to use at scale.

Unmodified C_{60} is already one of the most expensive materials in a perovskite solar cell, comprising 7% of the total material cost (~4.7% of overall manufacturing cost) despite making up only 3% of the overall thickness of the active materials.[8] Toughening strategies that require further chemical modification of the base C_{60} molecule are thus unlikely to be adopted by photovoltaic manufacturers as the costs of C_{60} derivatives are often substantially higher than that of the parent fullerene.

To address the shortcomings of C_{60}, researchers have investigated a broad range of both organic and inorganic non-fullerene acceptors (NFAs).[13-15] Amongst these NFAs, the naphthalene-diimide (NDI) functional group has attracted interest due to its tuneable energy levels and low absorbance in the visible light range. NDI-based small molecules and NDI polymers have been used in both normal (n-i-p) and inverted (p-i-n) perovskite solar cells as NFAs, but as with many other NFAs, NDI-based ETLs have struggled to reach the same efficiency and reproducibility as devices containing C_{60}-based ETLs, often due to insufficient charge-carrier mobility and high series resistance.[16-21] As mentioned above, researchers have mixed polymers with fullerenes in the past, however, most polymer-fullerene mixtures have been optimized at a very low polymer mass fraction. Studies have shown that polystyrene (PS) mixed with PC$_{60}$BM (a common C_{60} derivative developed for improved solution processability over C_{60}) at a composition of 1.5 wt% is

shown to reduce fullerene dimerization, and an ultra-thin passivation layer comprised of PC$_{60}$BM : poly-methylmethacrylate (PMMA) (2 : 1) has been used to decrease hysteresis.[22,23]

Rather than try to synthesize a new NDI molecule with improved electronic and mechanical properties to serve as an improved ETL, here we combine the electronic properties of C_{60} with the mechanical properties of a NDI-based polymer that blends well with C_{60} in solution and the solid state, allowing us to develop a fullerene-based ETL with polymer mass fractions up to 70%. We employed a side-chain NDI polymer, poly[*N*-(2-ethylhexyl)-*N'*-(2-(methacryloyloxy)ethyl)-naphthalene-1,8:4,5-bis(dicarboximide)] (pNDI, Fig. 1A), which is synthesized in five simple steps (Scheme S1), to create a solution-processable, mixed-polymer-C_{60} ETL with over 3× greater fracture energies than pure C_{60} for all tested polymer concentrations. Optimized devices with this ETL achieved a champion PCE of 26.1% and the optimized ETL exhibited an average fracture energy of 1.27 J m^{-2}. The similar reduction potential of pNDI to that of C_{60} ($E_{red,pNDI} = -1.08$ V *vs.* FeCp$_2^{+/0}$, Fig. S6, *vs.* $E_{red,C_{60}} = -0.98$ V) allows for a pNDI mass fraction of 50% without any negative effects on device PCE.[24] By partially substituting C_{60} ($625 g^{-1} at the research scale) with pNDI, this composite ETL approach introduces a potential avenue for cost reduction, contingent on further cost optimization of large-scale pNDI synthesis.

Results and discussion

We began our study by optimizing mixed-ETL spin-coating parameters to ensure homogenous films (Fig. S8). The optimization procedure considered total precursor solution concentration (including both C_{60} and pNDI), the mass fraction of pNDI in solution, and spin-coating speed. The optimization process involved visual inspection of films, atomic-force microscopy (AFM) for nano-scale film texture and uniformity (Fig. S7), and solar cell performance using a Cs$_{0.03}$(MA$_{0.03}$-FA$_{0.97}$)$_{0.97}$Pb(I$_{0.97}$Br$_{0.03}$)$_3$, 1.55 eV bandgap perovskite as the
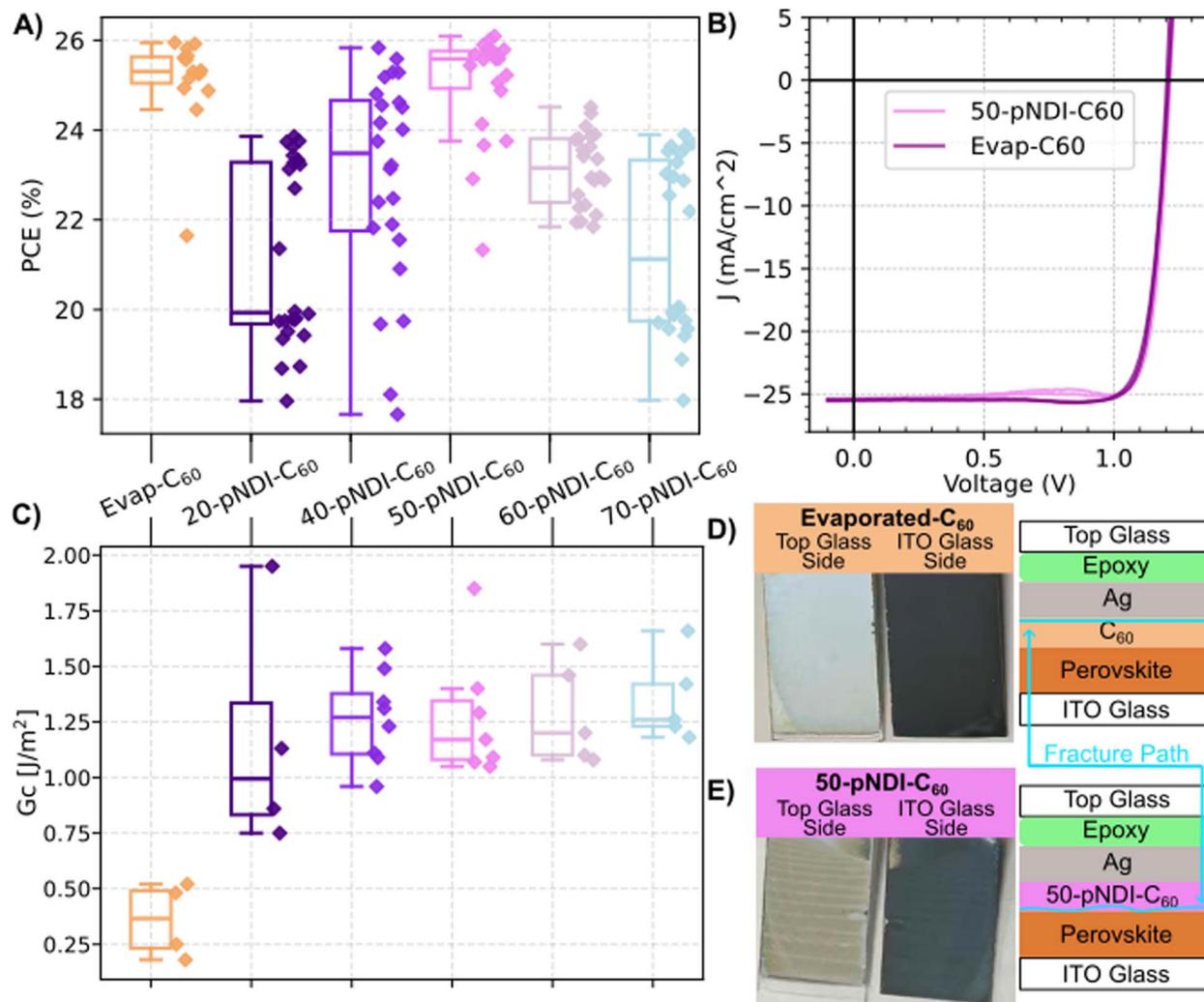
Fig. 2 (A) PCE boxplots for various compositions of x-pNDI-C_{60} compared to control, evaporated C_{60} devices. (B) JV curves of the champion control and x-pNDI-C_{60} devices. (C) Fracture energy box plots showing improvement when mixing increasing concentrations of pNDI into the C_{60} ETL. (D) Visual images of fracture surfaces of the 50-pNDI-C_{60} device and an illustration of fracture location. (E) Fracture surfaces of the control evaporated C_{60} sample and its fracture location in the sample.

photo absorber. The fracture energy was analyzed with glass-sandwiched samples in a double cantilever beam experiment where an initial crack is propagated, and subsequent cracks were analyzed as the sample was peeled apart, as depicted in Fig. 1B and C.

We found that an overall solution concentration of 25 mg ml^{-1} is optimal for spin-coating thin, smooth, mixed-polymer/fullerene ETL films. Optimal film thicknesses range from 25 nm to 40 nm depending on the polymer concentration (Table S1). Fig. 2A shows the PCE of cells fabricated with an architecture of tin-doped indium oxide (ITO)//4-[(3,6-dimethyl-9H-carbazol-9-yl)butyl]phosphonic acid (Me-4 PACz): 1,6-hexylene-diphosphonic acid (6dPa)//perovskite (PVK)//1,3-diaminopropane dihydroiodide (PDADI)//ETL//bathocuproine (BCP)//Ag, where the ETL is either thermally evaporated C_{60} or pNDI-C_{60} ETLs with a range of pNDI mass fractions between 20% and 70%. The highest PCEs (25.1 ± 1.19%) for cells using

blends were for those using 50% mass fraction pNDI, denoted 50-pNDI-C_{60}, virtually identical to the PCE of devices fabricated with pure evaporated C_{60} (25.1 ± 1.04%). Current density–voltage (JV) curves of pure C_{60} and 50-pNDI-C_{60} solar cells are shown in Fig. 2B. While the inclusion of 50 wt% pNDI preserves a stabilized PCE of >25%, it comes at the expense of a marginally increased spread of device performance compared to the thermally evaporated C_{60}—an expected finding for solution-processed films compared to the highly controlled, homogenous, and automated nature of thermal evaporation. In the 50-pNDI-C_{60} device JV curve, as seen in Fig. 2B, a "bump" is observed between 0.5 and 1 V. This can be attributed to polarization effects due to mobile ions and charge accumulation at the perovskite/ETL interface, but does not have a notable effect on PCE as seen by the maximum power point tracking (MPPT) curves in Fig. S17.[25] At the PCE-optimized pNDI concentration of 50%, the device's JV behaviour and performance is not

compromised, despite only 50% of the ETL volume being occupied by C_{60}. Cells fabricated with 50-pNDI-C_{60} and separately with evaporated C_{60} showed similar stability over 160 hours of accelerated aging using maximum-power point tracking in an aggressive 85 °C, 1-sun illumination environment (Fig. S18). Stability improvements may be expected since polymers have been seen to protect C_{60} from photo-induced dimerization and resulting degradation in electron mobilities.[26]

To determine whether the NDI moiety in the polymer helps retain the performance of the solar cell, we fabricated two other ETLs by using poly(methyl methacrylate) (PMMA) and polystyrene (PS) mixed with C_{60} at various concentrations (Fig. S20). A batch of these films on glass was first made and the film quality was assessed in a laser scanning confocal microscope (LSCM) in order to screen-out mixtures that did not deposit homogenous, pinhole-free films (Fig. S10). For all screened polymer concentrations of PMMA:C_{60} and PS:C_{60} mixed ETLs, the devices still worked as solar cells, but suffered from severe open-circuit voltage (V_{oc}) loss and high series resistance (Fig. S20 and 21). The poor PCE of these blends demonstrates that the polymer blending approach is not completely general: the difference between the behavior of pNDI and these other polymers might reflect the ability of the NDI groups to transport charges and/or differences in film morphology, perhaps associated with better miscibility between pNDI and C_{60} (as suggested by UV-vis. data showing pNDI reduces C_{60} aggregation more effectively than PS or PMMA, see below).[27]

Interestingly, for pNDI-C_{60} mixed ETLs, we see a continuous decrease in PCE as the polymer mass concentration is either lower or higher than 50%. We also observed increased variability of the PCE across cells fabricated in the same batch as the weight fraction of pNDI deviates from the optimal 50%. This can be attributed to unfavorable phase separation of the polymer and C_{60} phases. When the pNDI fraction exceeds 50%, charges are likely being extracted by the polymer more than by C_{60}, and the PCE loss as a result of low V_{oc} may be due to high surface recombination. When the pNDI fraction is less than 50%, C_{60} may aggregate in solution, which may lead to pinholes and inhomogeneity in the ETL. Pinholes in the ETL lead to areas in the device where the metal electrode contacts the perovskite directly, leading to V_{oc} losses and high recombination. The trends seen in the JV performance boxplots support these hypotheses (Fig. S16).

Because the critical stress for fracture in a thin-film sample is also dependent on fabrication quality and consistency (due to fabrication related defects such as pinholes, scratches, and impurity particles) two separate batches were made from different solutions and on different days. The aggregated, reproducible fracture energy results are shown in Fig. 2C. Aligning with values found in literature, our experimentation showed that the average fracture energy of samples fabricated with pure, thermally evaporated C_{60} ETL is 0.36 ± 0.07 J m^{-2}.[4–6] With as little as 20 wt% pNDI mixed into the ETL, the fracture energy increases to an average of 1.17 ± 0.11 J m^{-2}, a greater than 3× improvement over thermally evaporated C_{60}. As the weight fraction is gradually increased, an overall slow rise in fracture energy is observed. While the PCE-optimized ETL

composition of 50-pNDI-C_{60} does not exhibit the highest fracture energy—an average of 1.27 ± 0.06 J m^{-2}, compared to the average fracture energy seen in the 70-pNDI-C_{60} of 1.35 ± 0.07 J m^{-2}—the difference is negligible when compared to the substantial increase in fracture energy from the control, thermally evaporated C_{60} films. Recently, Schutt, et al. discussed findings from outdoor testing of commercial modules, where encapsulated Si/perovskite tandems failed in outdoor testing due to delamination of the C_{60}/tin oxide (SnO$_x$) interface when pure, evaporated C_{60} is used. However, fracture was not observed with a proprietary ETL with a G_c of 0.74 J m^{-2}.[10] Our data shows that our optimized 50-pNDI-C_{60} ETL's G_c is 0.53 J m^{-2} *tougher* than the proprietary ETL reported by Schutt, et al. that showed no delamination in indoor or outdoor aging tests.[10] Our results indicate that the improved G_c in our ETL could provide a large safety buffer against the mechanical driving forces leading to failure at the ETL when employed outdoors.

Beyond the *magnitude* of the fracture energy, the location of fracture also provides useful information. Fracture location was determined by visually inspecting the color of residual material on each fracture surface and confirmed with atomic depth sampling using a glow discharge optical emission spectrometer (Fig. S11 and 14). In samples prepared with pure C_{60}, as seen in Fig. 2D, the fracture occurs close to the C_{60}/Ag interface, indicating that the C_{60} is a "weak-link" in the device. For all of our tested pNDI:C_{60} compositions, fracture occurred closer to the pNDI-C_{60}/perovskite interface as depicted in Fig. 2E for the 50-pNDI-C_{60} composition (Fig. S11). Shifting of the fracture surface from near the silver interface to the perovskite interface implies strengthening of the top of the ETL stack. This adhesive strengthening at the interface may be a result of electrostatic interactions between the dipoles associated with the imide or acrylate functional groups in pNDI and the metallic silver film, whereas C_{60} only interacts with itself and with Ag through weak van der Waals interactions.[28,29] In some samples with pNDI concentrations of ≥60%, the fracture path crosses the interface and moves between the perovskite and the ETL (Fig. S12)—an indicator that at these concentrations, the G_c of our ETL is nearing that of the perovskite.

Optical characterization

Optical absorption spectra of the ETLs on glass are shown in Fig. 3A. pNDI shows weak, discrete absorption features only at wavelengths shorter than 400 nm. Nonetheless, all of the pNDI:C_{60} compositions show less optical absorptance than evaporated C_{60} despite some of the pNDI:C_{60} films being thicker. For example, the optimized 50-pNDI-C_{60} (Fig. 3A) film is ∼34 nm thick (Table S1), about 9 nm thicker than the evaporated C_{60} film. The reduction in absorptance is therefore due to the low concentration of C_{60} in the pNDI-C_{60} films and the low absorptance of the pNDI, together giving the mixed material a lower absorption coefficient than pure C_{60}. While this is not immediately beneficial for single-junction inverted perovskite solar cells (where incident light enters through the hole-extracting side of the device), reduced parasitic absorption in a C_{60}-based ETL is notable for Si-perovskite tandem solar
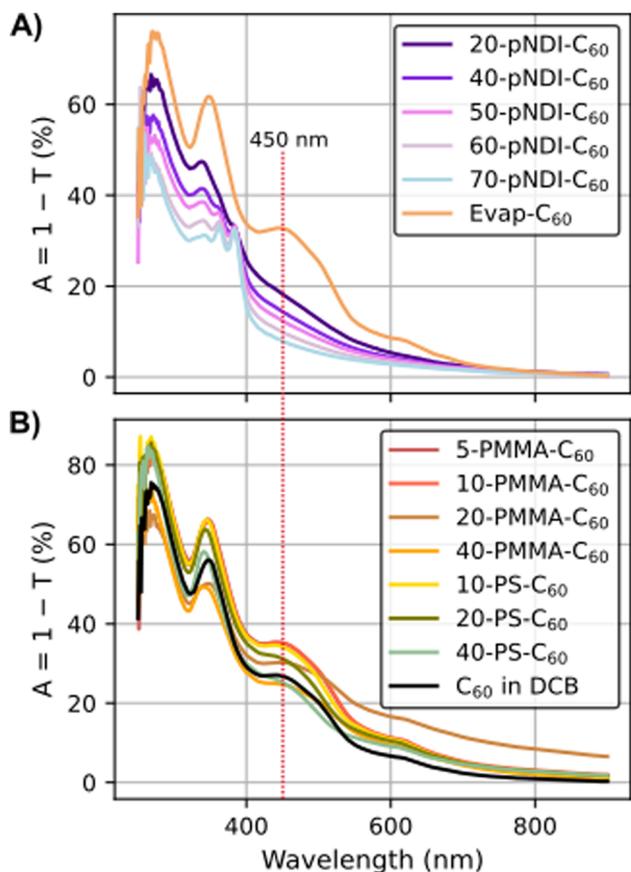
Fig. 3 Optical absorption spectra of: (A) thermally evaporated C_{60} ("Evap-C_{60}") and x-pNDI-C_{60} mixed-polymer ETLs. (B) Spin-coated C_{60} ("C_{60} in DCB") and x-PMMA-C_{60} and x-PS-C_{60} mixed-polymer ETLs. Red dotted vertical line highlights an absorption feature associated with aggregated C_{60}.

cells.[30,31] The pNDI-C_{60} films transmit about 12% more optical power from an AM1.5G spectrum than evaporated C_{60} between 280 nm and 750 nm (Fig. S13). Considering a simple Si-perovskite tandem solar cell with a 1.67 eV perovskite top-cell (with an architecture of cover glass//ethylene-vinyl acetate (EVA) encapsulant//ITO//ETL//PVK), we calculate that the reduced parasitic absorption with 50-pNDI-C_{60} would result in a 11% greater short-circuit current density over a device with an evaporated C_{60} ETL (SI Section S6).

Besides the benefit of reduced parasitic absorption, the pNDI-C_{60} system also reduces C_{60} aggregation, a feature that can be analysed from the absorption peak at 450 nm (Fig. 3A, vertical red line).[32] With increasing polymer concentration, a significant suppression of the absorption "shoulder" at 450 nm is observed, indicating that pNDI prevents micron-scale C_{60} aggregation in the solid ETL film, resulting in a homogenously mixed film. The absence of these aggregates in the ETL may also reduce the energetic disorder of C_{60} and thus support electron transport in the film.[33,34]

To assess the importance of the NDI group in suppressing C_{60} aggregation, further optical absorption spectra were taken on the PMMA:C_{60} and PS:C_{60} ETL systems discussed previously.

Fig. 3B shows that for any of the tested concentrations of PMMA or PS, and in solution-processed pure C_{60}, the absorption peak at 450 nm persists. This suggests that most of the aggregation suppression induced by pNDI is not simply due to the polymeric nature of this material, but favorable polar or dispersive interactions between the C_{60} and the pNDI.

Conclusions

We have shown that mixing pNDI with C_{60}-fullerene at a mass fraction of 50% produces a mechanically robust ETL with a fracture energy over $3\times$ higher than that of pure, thermally evaporated C_{60}, without detrimental impacts on device performance. While these benefits are directly applicable to improving the durability of single-junction perovskite solar cells, the added benefit of reducing parasitic absorption makes this ETL an excellent candidate for high efficiency Si-perovskite tandem solar cells. We estimate that, with an optimized process and not taking into account other costs such as labor and purification, the material cost of pNDI could be \$10 g^{-1} (Table S4). This is significantly lower than the price of C_{60} at the research scale and likely lower than what C_{60} may cost at commercial scales. Additionally, the most common solution processable fullerene, PC$_{60}$BM, is around $10\times$ the cost of C_{60}, making our solution an economical choice for solution processable fullerenes. All of this makes our PCE optimized ETL, 50-pNDI-C_{60}, an excellent material candidate in the drive to make perovskite solar cells more cost-effective.

Experimental

Synthesis and characterization

Materials synthesis. pNDI was synthesized as described in the SI.

Mechanical testing. The double cantilever beam (DCB) test is a widely used fracture-mechanics-based technique for quantitatively evaluating the adhesion and interfacial fracture behavior of thin-film materials and multilayer stacks.[35–37] Our DCB samples adopted a structure of glass/1.55 eV PVK/ETL/Ag/epoxy/glass. The epoxy used was Loctite epoxy instant mix 5 min, which was applied to the top substrate (bare glass) and bonded to the bottom glass substrate (deposited with materials). Specific details of the testing method can be found elsewhere.[4,38,39] Briefly, a pre-crack was introduced into the DCB sample along the orientation of the crack propagation by inserting the tip of a razor blade into the DCB sample. The resulting pre-crack can protect the DCB sample from excessive tensile loads and initiate crack propagation. By using the delaminator system (DTS, USA), the cracked DCB samples were mounted and loaded in tension at a displacement rate of 1 μm s^{-1}. When a unit of well-defined mode I fracture occurred, the DCB sample was partially unloaded to calculate the compliance and loaded again to gradually propagate the crack until a complete separation was achieved for the two bonded glass substrates, suggesting the completion of measurement. In the measurement, the load (P) – displacement (n) curves were

continuously recorded and used to extract the fracture energy (G_c), which can be calculated by the following equation:[40]

$$G_c = \frac{12 P_c^2 a^2}{B^2 E' h^3} \left(1 + 0.64 \frac{h}{a}\right)^2 \qquad (1)$$

where P_c is the critical load that deviates from the linearity in the $P–n$ curve during the loading cycle; a is the crack length; B and h are the width and half height of the sample, respectively; and E' is the plane-strain elastic modulus of the substrate. The crack length was estimated by the following compliance method:

$$a = \left(\frac{d\Delta}{dP} \cdot \frac{B E' h^3}{8}\right)^{\frac{1}{3}} - 0.64 h \qquad (2)$$

where n is the displacement and P is the applied load. The G_c tests were carried out in laboratory air environment at ~20 °C and ~20% R. H.

GDOES measurement. Elemental depth profiling was performed using a Horiba GD-Profiler 2 Glow Discharge Optical Emission Spectrometer (GDOES). Measurements were performed on delaminated DCB samples at room temperature to determine the relative presence of key elements. Plasma sputtering was performed in radio-frequency mode at 15 W, ensuring stable plasma operation. Emission signals from C were tracked to indicate the presence of C_{60}, Ag signals were used to identify the presence of silver, and Pb signals were monitored to confirm the perovskite layer.

Current density *vs.* voltage scans and MPPT measurements were taken under illumination from a Pico G2V solar simulator in an N_2 environment and using a Keithley 2400 Source Measure Unit.

Optical absorption spectra were derived from transmittance spectra measured using a PerkinElmer Lambda 35 UV-vis spectrometer.

X-ray diffraction was performed with a Rigaku Smartlab 9 kW diffractometer.

Accelerated long-term stability measurements were performed in a Fluxim LitosLite multi-channel stability tester. Samples were held at 85 °C while the system's maximum-power-point tracking (MPPT) protocol was continuously performed under the nominal 1-sun AM1.5G simulated solar spectrum. Cells were illuminated through a shadow mask with a nominal area of 0.058 cm² (squares). Data recording point rate 0.5 1/min. A light-IV scan was run once every 2 hours to track JV parameters.

Device fabrication

Perovskite solar cells were made with an inverted, *p-i-n* architecture of ITO//Me4PACz:6dPA//1.55 eV PVK//PDADI//ETL//BCP//Ag. Patterned indium tin oxide (ITO) glass was purchased from Delta Technologies and cleaned thoroughly in three consecutive sonicated baths of de-ionized water, acetone, and IPA, each for 20 minutes. The ITO substrates were UV-ozone treated for 20 min prior to spin-coating. All spin-coating and annealing parameters are outlined in Table S3. For the hole transport layer (HTL), a 4 : 1 (v : v) solution of Me4PACz (1 mg mL⁻¹ in EtOH, TCI America) and 1,6-hexylenediphosphonic acid (0.75 mg mL⁻¹ in EtOH, TCI America) was sonicated before use and spin-coated onto the ITO glass then treated with an annealing step. The perovskite had a 1.55 eV bandgap and a composition of $Cs_{0.03}(MA_{0.3}FA_{0.97})_{0.97}Pb(I_{0.97}Br_{0.03})_3$. The precursor solution was made by weighing precise amounts of the following salts in a 1 mL solvent system of 4 : 1 (v/v) DMF : DMSO to form a 1.5 M solution of $Cs_{0.03}(MA_{0.3}FA_{0.97})_{0.97}Pb(I_{0.97}Br_{0.03})_3$: methylammonium bromide (Sigma-Aldrich), CsI (Sigma-Aldrich), PbBr₂ (Sigma-Aldrich), formamidiniuim iodide (Great Cell Solar), and PbI₂ (TCI America).

The perovskite film was passivated by spin-coating a 2 mg mL⁻¹ solution of propane-1,3-diammonium diiodide ("PDADI", Great Cell Solar) in IPA followed by annealing. Finally, 60 μL of the x-pNDI-C_{60} ETL was spin-coated as a 25 mg mL⁻¹ solution in dichlorobenzene. For devices with thermally evaporated C_{60}, the substrates were moved into an Angstrom Engineering thermal evaporator, and 25 nm of C_{60} was deposited on top of the PDADI passivation. A 6-nm-thick hole blocking layer of bathocuproine ("BCP", TCI America) was then thermally evaporated. Lastly 150 nm of Ag (Kurt J. Lesker Company) was thermally evaporated to finish the devices.

All solutions and devices were made in gloveboxes with controlled nitrogen environments with O_2 levels at <0.1 ppm and moisture content at <0.1 ppm.

Author contributions

Conceptualization: S. M., M. D. M., Y. Z., S. B.; polymer synthesis: Y. Z.; validation: M. R. S. P., K. M., M. L.; formal analysis: M. R. S. P., K. M., M. L., N. R.; investigation: M. R. S. P., M. L., Y. Z.; data curation: M. R. S. P., M. L., R. D.; writing – original draft: M. R. S. P., writing – review & editing: all co-authors.

Conflicts of interest

Prof. Mike McGehee is an advisor to Swift Solar. The University of Colorado filed a provisional patent on the work described herein.

Data availability

All supporting data for this article have been included in the supplementary information (SI). Data supporting the analyses in this article are available through Mendelay Data at DOI: https://doi.org/10.17632/y8g28btd85.1. Supplementary information is available. See DOI: https://doi.org/10.17632/y8g28btd85.1.

Acknowledgements

References

1 M. A. Green, E. D. Dunlop, M. Yoshita, N. Kopidakis, K. Bothe, G. Siefer, D. Hinken, M. Rauer, J. Hohl-Ebinger and X. Hao, Solar Cell Efficiency Tables (Version 64), *Prog. Photovoltaics Res. Appl.*, 2024, **32**(7), 425–441, DOI: 10.1002/PIP.3831.

2 W. Peng, K. Mao, F. Cai, H. Meng, Z. Zhu, T. Li, S. Yuan, Z. Xu, X. Feng, J. Xu, M. D. McGehee and J. Xu, Reducing Nonradiative Recombination in Perovskite Solar Cells with a Porous Insulator Contact, *Science*, 2023, **379**(6633), 683–690, DOI: 10.1126/SCIENCE.ADE3126/SUPPL_FILE/SCIENCE.ADE3126_SIMULATION_MODEL_FILE.ZIP.

3 R. Zahran and Z. Hawash, Fullerene-Based Inverted Perovskite Solar Cell: A Key to Achieve Promising, Stable, and Efficient Photovoltaics, *Adv. Mater. Interfaces*, 2022, **9**(35), 2201438, DOI: 10.1002/ADMI.202201438.

4 M. Li, S. Johnson, L. Gil-Escrig, M. Sohmer, C. A. Figueroa Morales, H. Kim, S. Sidhik, A. Mohite, X. Gong, L. Etgar, H. J. Bolink, A. Palmstrom, M. D. McGehee and N. Rolston, Strategies to Improve the Mechanical Robustness of Metal Halide Perovskite Solar Cells, *Energy Adv.*, 2024, **3**(1), 273–280, DOI: 10.1039/D3YA00377A.

5 M. Casareto and N. Rolston, Designing Metal Halide Perovskite Solar Modules for Thermomechanical Reliability, *Commun. Mater.*, 2024, **5**(1), 1–6, DOI: 10.1038/s43246-024-00515-2.

6 B. L. Watson, N. Rolston, K. A. Bush, T. Leijtens, M. D. McGehee and R. H. Dauskardt, Cross-Linkable, Solvent-Resistant Fullerene Contacts for Robust and Efficient Perovskite Solar Cells with Increased JSC and VOC, *ACS Appl. Mater. Interfaces*, 2016, **8**(39), 25896–25904, DOI: 10.1021/ACSAMI.6B06164.

7 J. J. Cordell, M. Woodhouse and E. L. Warren, Technoeconomic Analysis of Perovskite/Silicon Tandem Solar Modules, *Joule*, 2025, **9**(2), 101781, DOI: 10.1016/J.JOULE.2024.10.013.

8 Y. Liu, Z. Zhang, T. Wu, W. Xiang, Z. Qin, X. Shen, Y. Peng, W. Shen, Y. Li and L. Han, Cost Effectivies Analysis of Perovskite Solar Cells: Will It Outperform Crystalline Silicon Ones?, *Nanomicro Lett.*, 2025, **17**(1), 1–11, DOI: 10.1007/S40820-025-01744-X/FIGURES/7.

9 Z. Dai and N. P. Padture, Challenges and Opportunities for the Mechanical Reliability of Metal Halide Perovskites and Photovoltaics, *Nat. Energy*, 2023, **8**(12), 1319–1327, DOI: 10.1038/S41560-023-01378-6;SUBJMETA.

10 K. Schutt, M. Davis, M. Li, S. A. Johnson, D. Martinez, J. Titus, T. Leijtens, B. Martin, M. D. Mcgehee, S. R. Marder, N. Rolston and J. M. Luther, Toward Fullerene-Free PIN Perovskite Solar Cells, *ACS Energy Lett.*, 2025, **10**(12), 6307–6317, DOI: 10.1021/acsenergylett.5c02987.

11 S. You, H. Zhu, Z. Shen, X. Wang, B. Shao, Q. Wang, J. Lu, Y. Yuan, B. D. Dou, E. M. Sanehira, T. Russell, A. Lorenz, Y. Dong, L. Chen, M. Casareto, N. Rolston, M. C. Beard, J. J. Berry, M. Freitag, Y. Yan, O. M. Bakr and K. Zhu, C60-Based Ionic Salt Electron Shuttle for High-Performance Inverted Perovskite Solar Modules, *Science*, 2025, **388**(6750), 964–968, DOI: 10.1126/SCIENCE.ADV4701.

12 Z. Xing, S. Ma, B. Chen, M. An, A. Fan, X. Hu, Y. Wang, L. Deng, Q. Huang, H. Kanda, F. G. Al-amri, G. Pozzi, Y. Zhang, J. Xia, J. Wu, X. Guo and M. K. Nazeeruddin, Solubilizing and Stabilizing C60 with N-Type Polymer Enables Efficient Inverted Perovskite Solar Cells, *Joule*, 2025, **9**(4), 101817, DOI: 10.1016/J.JOULE.2024.101817.

13 S. Pont, F. Foglia, A. M. Higgins, J. R. Durrant, J. T. Cabral, S. Pont, J. R. Durrant, J. T. Cabral, F. Foglia and A. M. Higgins, Stability of Polymer:PCBM Thin Films under Competitive Illumination and Thermal Stress, *Adv. Funct. Mater.*, 2018, **28**(40), 1802520, DOI: 10.1002/ADFM.201802520.

14 X. Huang, D. Xia, Q. Xie, D. Wang, Q. Li, C. Zhao, J. Yin, F. Cao, Z. Su, Z. Zeng, W. Jiang, W. Kaminsky, K. Liu, F. R. Lin, Q. Feng, B. Wu, S. W. Tsang, D. Lei, W. Li and A. K. Y. Jen, Supramolecular Force-Driven Non-Fullerene Acceptors as an Electron-Transporting Layer for Efficient Inverted Perovskite Solar Cells, *Nat. Commun.*, 2025, **16**(1), 1–11, DOI: 10.1038/S41467-025-56060-0;TECHMETA.

15 D. S. Utomo, L. M. Svirskaite, A. Prasetio, V. Malinauskiene, P. Dally, E. Aydin, A. Musiienko, V. Getautis, T. Malinauskas, R. Azmi and S. De Wolf, Nonfullerene Self-Assembled Monolayers As Electron-Selective Contacts for n-i-p Perovskite Solar Cells, *ACS Energy Lett.*, 2024, **9**(4), 1682–1692, DOI: 10.1021/ACSENERGYLETT.4C00306.

16 M. A. Jameel, T. C. J. Yang, G. J. Wilson, R. A. Evans, A. Gupta and S. J. Langford, Naphthalene Diimide-Based Electron Transport Materials for Perovskite Solar Cells, *J. Mater. Chem. A*, 2021, **9**(48), 27170–27192, DOI: 10.1039/D1TA08424K.

17 X. Li, W. Wang, P. Huang, L. Yang, J. Hu, K. Wei, L. Gao, Y. Jiang, K. Sun, G. Du, X. Cai, C. Liu, W. Tang and J. Zhang, Fluorinated Naphthalene Diimides as Buried Electron Transport Materials Achieve Over 23% Efficient Perovskite Solar Cells, *Advanced Science*, 2024, **11**(36), 2403735, DOI: 10.1002/ADVS.202403735.

18 J. H. Heo, S. C. Lee, S. K. Jung, O. P. Kwon and S. H. Im, Efficient and Thermally Stable Inverted Perovskite Solar Cells by Introduction of Non-Fullerene Electron Transporting Materials, *J. Mater. Chem. A*, 2017, **5**(39), 20615–20622, DOI: 10.1039/C7TA06900F.

19 Y. Shi, D. P. McCarthy, D. Lungwitz, F. Jiang, M. Taddei, H. Contreras, Y. Lin, A. A. Mohapatra, K. Tang, Y. Zhang, S. Barlow, A. Kahn, S. R. Marder and D. S. Ginger, Photo-Crosslinkable Naphthalene Diimide Polymer for Solution-Processed n–i–p Perovskite Solar Cells, *Chem. Mater.*, 2024, **36**(2), 795–802, DOI: 10.1021/ACS.CHEMMATER.3C02295.

20 K. Al Kurdi, D. P. McCarthy, D. P. McMeekin, S. O. Furer, M. H. Tremblay, S. Barlow, U. Bach and S. R. Marder, A Naphthalene Diimide Side-Chain Polymer as an Electron-Extraction Layer for Stable Perovskite Solar Cells, *Mater.*

Chem. Front., 2021, **5**(1), 450–457, DOI: 10.1039/D0QM00685H.

21 C. Sun, Z. Wu, H. L. Yip, H. Zhang, X. F. Jiang, Q. Xue, Z. Hu, Z. Hu, Y. Shen, M. Wang, F. Huang and Y. Cao, Amino-Functionalized Conjugated Polymer as an Efficient Electron Transport Layer for High-Performance Planar-Heterojunction Perovskite Solar Cells, *Adv. Energy Mater.*, 2016, **6**(5), 1501534, DOI: 10.1002/AENM.201501534.

22 Y. Bai, H. Yu, Z. Zhu, K. Jiang, T. Zhang, N. Zhao, S. Yang and H. Yan, High Performance Inverted Structure Perovskite Solar Cells Based on a PCBM:Polystyrene Blend Electron Transport Layer, *J. Mater. Chem. A*, 2015, **3**(17), 9098–9102, DOI: 10.1039/C4TA05309E.

23 X. Hu, H. Wang, M. Wang and Z. Zang, Interfacial Defects Passivation Using Fullerene-Polymer Mixing Layer for Planar-Structure Perovskite Solar Cells with Negligible Hysteresis, *Sol. Energy*, 2020, **206**, 816–825, DOI: 10.1016/J.SOLENER.2020.06.057.

24 M. Hayakawa, N. Sunayama, S. I. Takagi, Y. Matsuo, A. Tamaki, S. Yamaguchi, S. Seki and A. Fukazawa, Flattened 1D Fragments of Fullerene C60 That Exhibit Robustness toward Multi-Electron Reduction, *Nat. Commun.*, 2023, **14**(1), 1–12, DOI: 10.1038/s41467-023-38300-3.

25 G. De Moor, N. Charvin, C. Farha, T. Meyer, L. Perrin, E. Planes and L. Flandin, Understanding the Anomalous J–V Curves in Carbon-Based Perovskite Solar Cells as a Structural Transition Induced by Ion Diffusion, *Sol. RRL*, 2024, **8**(8), 2300998, DOI: 10.1002/SOLR.202300998.

26 T. Heumueller, W. R. Mateker, A. Distler, U. F. Fritze, R. Cheacharoen, W. H. Nguyen, M. Biele, M. Salvador, M. Von Delius, H. J. Egelhaaf, M. D. McGehee and C. J. Brabec, Morphological and Electrical Control of Fullerene Dimerization Determines Organic Photovoltaic Stability, *Energy Environ. Sci.*, 2016, **9**(1), 247–256, DOI: 10.1039/C5EE02912K.

27 N. R. Tummala, S. G. Aziz, V. Coropceanu and J. L. Bredas, Characterization of the Structural, Mechanical, and Electronic Properties of Fullerene Mixtures: A Molecular Simulations Description, *J. Mater. Chem. C*, 2018, **6**(14), 3642–3650, DOI: 10.1039/C7TC03820H.

28 S. C. Park, S. S. Yoon and J. D. Nam, Surface Characteristics and Adhesive Strengths of Metal on O2 Ion Beam Treated Polyimide Substrate, *Thin Solid Films*, 2008, **516**(10), 3028–3035, DOI: 10.1016/J.TSF.2007.11.113.

29 M. Heydari, F. Sharif and M. Ebrahimi, A Molecular Dynamics Study on the Role of Oxygen-Containing Functional Groups on the Adhesion of Polymeric Films to the Aluminum Surface, *Fluid Phase Equilib.*, 2021, **536**, 112966, DOI: 10.1016/J.FLUID.2021.112966.

30 Q. Q. Chu, B. Cheng and B. Fang, Scalable and Efficient All-Perovskite Tandem Solar Cells, *Matter*, 2022, **5**(9), 2584–2586, DOI: 10.1016/J.MATT.2022.07.026.

31 A. A. Said, E. Aydin, E. Ugur, Z. Xu, C. Deger, B. Vishal, A. Vlk, P. Dally, B. K. Yildirim, R. Azmi, J. Liu, E. A. Jackson, H. M. Johnson, M. Gui, H. Richter, A. R. Pininti, H. Bristow, M. Babics, A. Razzaq, T. G. Allen, M. Ledinský, I. Yavuz, B. P. Rand and S. De Wolf, Sublimed C60 for Efficient and Repeatable Perovskite-Based Solar Cells, *Nat. Commun.*, 2024, **15**(1), 1–10, DOI: 10.1038/s41467-024-44974-0.

32 N. O. McHedlov-Petrossyan, Fullerenes in Liquid Media: An Unsettling Intrusion into the Solution Chemistry, *Chem. Rev.*, 2013, **113**(7), 5149–5193, DOI: 10.1021/CR3005026.

33 Y. Jiang, J. Wang, H. Zai, D. Ni, J. Wang, P. Xue, N. Li, B. Jia, H. Lu, Y. Zhang, F. Wang, Z. Guo, Z. Bi, H. Xie, Q. Wang, W. Ma, Y. Tu, H. Zhou and X. Zhan, Reducing Energy Disorder in Perovskite Solar Cells by Chelation, *J. Am. Chem. Soc.*, 2022, **144**(12), 5400–5410, DOI: 10.1021/JACS.1C12732.

34 N. R. Tummala, Z. Zheng, S. G. Aziz, V. Coropceanu and J. L. Brédas, Static and Dynamic Energetic Disorders in the C60, PC61BM, C70, and PC71BM Fullerenes, *J. Phys. Chem. Lett.*, 2015, **6**(18), 3657–3662, DOI: 10.1021/ACS.JPCLETT.5B01709.

35 B. Dong, M. Wei, Y. Li, Y. Yang, W. Ma, Y. Zhang, Y. Ran, M. Cui, Z. Su, Q. Fan, Z. Bi, T. Edvinsson, Z. Ding, H. Ju, S. You, S. M. Zakeeruddin, X. Li, A. Hagfeldt, M. Grätzel and Y. Liu, Self-Assembled Bilayer for Perovskite Solar Cells with Improved Tolerance against Thermal Stresses, *Nat. Energy*, 2024, **10**(3), 342–353, DOI: 10.1038/s41560-024-01689-2.

36 N. P. Padture, Trade-Offs at the Interface, *Nat. Energy*, 2025, **10**(2), 153–154, DOI: 10.1038/s41560-024-01691-8.

37 Z. Dai, S. K. Yadavalli, M. Chen, A. Abbaspourtamijani, Y. Qi and N. P. Padture, Interfacial Toughening with Self-Assembled Monolayers Enhances Perovskite Solar Cell Reliability, *Science*, 2021, **372**(6542), 618–622, DOI: 10.1126/SCIENCE.ABF5602/SUPPL_FILE/ABF5602_DAI_SM.

38 Z. Dai, S. K. Yadavalli, M. Chen, A. Abbaspourtamijani, Y. Qi and N. P. Padture, Interfacial Toughening with Self-Assembled Monolayers Enhances Perovskite Solar Cell Reliability, *Science*, 2021, **372**(6542), 618–622, DOI: 10.1126/science.abf5602.

39 N. Rolston, A. D. Printz, J. M. Tracy, H. C. Weerasinghe, D. Vak, L. Jia Haur, A. Priyadarshi, N. Mathews, D. J. Slotcavage, M. D. McGehee, R. E. Kalan, K. Zielinski, R. L. Grimm, H. Tsai, W. Nie, A. D. Mohite, S. Gholipour, M. Saliba, M. Grätzel, R. H. Dauskardt, N. Rolston, A. D. Printz, J. M. Tracy, D. J. Slotcavage, M. D. McGehee, R. H. Dauskardt, H. C. Weerasinghe, D. Vak, L. J. Haur, A. Priyadarshi, N. Mathews, R. E. Kalan, K. Zielinski, R. L. Grimm, H. Tsai, W. Nie, A. D. Mohite, S. Gholipour, M. Saliba and M. Grätzel, Effect of Cation Composition on the Mechanical Stability of Perovskite Solar Cells, *Adv. Energy Mater.*, 2018, **8**(9), 1702116, DOI: 10.1002/AENM.201702116.

40 M. F. Kanninen, An Augmented Double Cantilever Beam Model for Studying Crack Propagation and Arrest, *Int. J. Fract.*, 1973, **9**(1), 83–92, DOI: 10.1007/BF00035958.